



**HAL**  
open science

## On evaporation via an inclined rotating circular lift-off shadow or stencil mask

S. Arscott

► **To cite this version:**

S. Arscott. On evaporation via an inclined rotating circular lift-off shadow or stencil mask. *Journal of Vacuum Science & Technology B Microelectronics and Nanometer Structures*, 2019, 37 (1), pp.011602. 10.1116/1.5057404 . hal-02345344

**HAL Id: hal-02345344**

**<https://hal.science/hal-02345344>**

Submitted on 6 Jan 2021

**HAL** is a multi-disciplinary open access archive for the deposit and dissemination of scientific research documents, whether they are published or not. The documents may come from teaching and research institutions in France or abroad, or from public or private research centers.

L'archive ouverte pluridisciplinaire **HAL**, est destinée au dépôt et à la diffusion de documents scientifiques de niveau recherche, publiés ou non, émanant des établissements d'enseignement et de recherche français ou étrangers, des laboratoires publics ou privés.

# On evaporation via an inclined rotating circular

## *lift-off* shadow or stencil mask

Steve Arscott

*Institut d'Electronique, de Microélectronique et de Nanotechnologie (IEMN), CNRS UMR8520,  
The University of Lille, Cité Scientifique, Avenue Poincaré, 59652 Villeneuve d'Ascq, France*

Electronic mail: [steve.arscott@iemn.univ-lille1.fr](mailto:steve.arscott@iemn.univ-lille1.fr)

A mathematical model is developed to calculate the topography of a mesa obtained by evaporation of matter via inclined rotating *lift-off* shadow masking. Two types of masking are considered: a circular mask and a cylindrical mask—the latter involves sidewall deposition. The model is able to predict various topographic profiles obtained via the evaporative deposition of matter, e.g. metals, when using a physical mask, e.g. a photoresist or an electron beam-sensitive resist patterned onto a flat wafer. The model predicts a range of profiles, e.g. sharp cones, round-tipped cones, spikes, irregular bumps, flat-topped features, ‘bagel-shaped’ features, flat rings, and cylinders (fixed to the wafer and releasable)—depending on the aspect ratio of the circular opening, the deposition thickness, and the evaporation tilt angle. The ideas are extended to model an idealized resist-based *lift-off* mask involving overhang and undercut features. The model is simple to implement and should be of use for predicting the shape of deposited matter when using *lift-off* and stencil procedures—even at sub-micrometre dimensions. Despite its simplicity, the model goes some way in helping to understand the sensitivity of the various parameters on the final topography of the deposited matter. For example, the tilt angle—even when small—has an influence on the curvature radius of cone tips. In this

way, the prediction—and even optimization—of the shape of the deposited material is possible prior to embarking on time-consuming, and perhaps costly, experimentation.

## I. INTRODUCTION

The ability to control the shape of small material features at the nanometre scale<sup>1</sup> is important in many areas of technology ranging from transistor technologies<sup>2–5</sup> and small sharp points<sup>6–9</sup> for a variety of near-field microscopies, to arrays of mesas for metamaterials and photonics.<sup>10–13</sup> The patterning of materials, e.g. a thin film metal, onto a flat surface, e.g. a polished semiconductor wafer, is commonly done by physical vapour deposition (PVD), e.g. thermal evaporation, via a physical mask.<sup>2</sup> This physical mask is usually some form of spin-coated polymer thin film—often referred to simply as the ‘*resist*’—and patterned using either photolithography or electron beam lithography. The resist profile normally involves the formation of an overhanging feature—to achieve a shadowing effect—obtained by *undercutting* the resist during development. Following the deposition of the matter, the resist is removed, i.e. the so-called *lift-off* process,<sup>14–18</sup> to leave the required material patterns on the wafer surface. In order to control thin film uniformity,<sup>19</sup> the wafer is often rotated<sup>20</sup> and can be inclined during evaporation.<sup>21</sup> In the *lift-off* process, the aspect ratio and profile of the resist opening play a key role in determining the influence of *edge effects*, e.g. shadowing, on the final structure—such edge effects are critical in the fabrication of modern microelectronics.<sup>2,4</sup> If the aspect ratio of the resist opening is large, as in the case of tall narrow patterning, then shadowing effects will be important. This can result in small, conic-like features being formed after *lift-off*—even if the wafer is not intentionally inclined—due to some lateral deposition

closing the resist opening. Determining the topographic profile of the deposition when the wafer contains arbitrary geometry, high-aspect-ratio openings, under rotation and inclination is not trivial<sup>22</sup>—with several solutions having been proposed which make use of numerical methods.<sup>23–33</sup> The main parameters in this process are: the resist thickness, the resist opening width, the resist profile, the evaporation angle, the evaporated material thickness, the lateral sidewall and vertical evaporation onto the mask itself.

## II. Evaporation via a *lift-off* or stencil mask

In order to model the deposition topography resulting from the evaporation, this relatively complex situation—due to the variety of practical *lift-off* profiles—can be greatly simplified as either: (i) A mask composed as a circular hole at a distance above the wafer [see Fig 1(a)]—as would be, for example, the practical case of a ‘stencil’ mask<sup>34,35</sup> or (ii) a perfect cylindrical opening [see Fig. 1(b)]—the sidewalls in the latter are solid and perfectly vertical—as would be the case of an ideal resist opening.

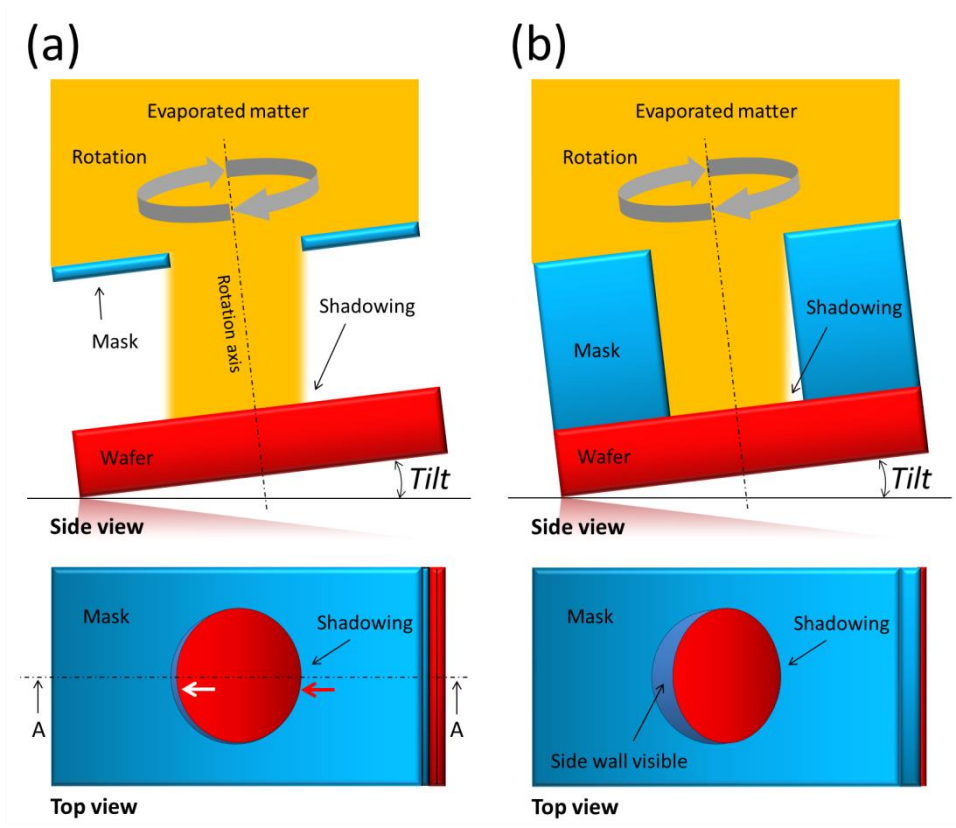


FIG. 1. (Color online) Physical vapour deposition via masking showing the effect of shadowing. (a) A circular hole and (b) a cylindrical opening. The evaporated matter (e.g. gold) passes through the circular stencil or *lift-off* masking (blue) and is deposited onto the wafer surface (red). In the case of a cylindrical masking, deposition also occurs on the sidewalls. The axis of the mask/wafer ensemble rotation is perpendicular to the wafer surface (indicated by a black dashed line).

Let us first describe intuitively what is happening as the evaporation proceeds. As the tilted wafer is rotated, matter will be deposited onto the exposed wafer surface, the top of the mask, and the exposed sidewalls—the latter occurs in the case of the

cylindrical opening. During a single revolution, the amount of matter deposited at a single point (either on the wafer surface or on the sidewalls) will depend how long that point is not in the shadow of the mask. In addition, during the evaporation the surface of the mask is also being deposited with matter, its dimensions are thus changing—this too, along with the inclined rotation, affects the shadowing as the deposition proceeds.

In the case of the circular opening, we will try to develop a solution for the thickness of deposited matter along the surface of the wafer, in terms of the mask dimensions, the evaporation tilt angle, and the total evaporation thickness. In the case of the cylindrical opening, we will also try to provide a solution for the thickness of deposited matter on the sidewalls, in terms of the mask dimensions, the evaporation tilt angle, and the total evaporation thickness.

### **III. A MODEL FOR THE TOPOGRAPHY OF AN EVAPORATED MESA ON THE WAFER SURFACE**

#### ***A. Basic assumptions***

In order to move forward, we must first make some basic assumptions. We assume that the evaporation rotational speed is large enough to allow *at least one whole revolution* of the tilted mask and wafer during the evaporation—in practice, several rotations are usually performed during the evaporation of typical thicknesses of matter involved i.e. 10 nm to 1000 nm. We assume that the evaporation tilt angle is constant during the deposition of the matter and that the mask (circular or cylindrical) rotates about the axis of the circle or cylinder. We assume that the evaporation source-to-wafer

distance is much larger than the mask dimensions and the spacing of the features on the mask. We assume that the matter is deposited evenly over the patterns.<sup>36</sup> We assume that the evaporated matter arrives in straight lines from the source. We assume that the evaporation rate and deposition rate of the matter are constant during the evaporation. Finally, physical issues<sup>37,38</sup> such as the material's granularity<sup>39</sup> or migration of species on the wafer surface<sup>40</sup> are not taken into account.

### ***B. Development of the model***

The practical masking and setup shown in Fig. 1 can be replaced by simple schematic stick figures shown in Fig. 2.

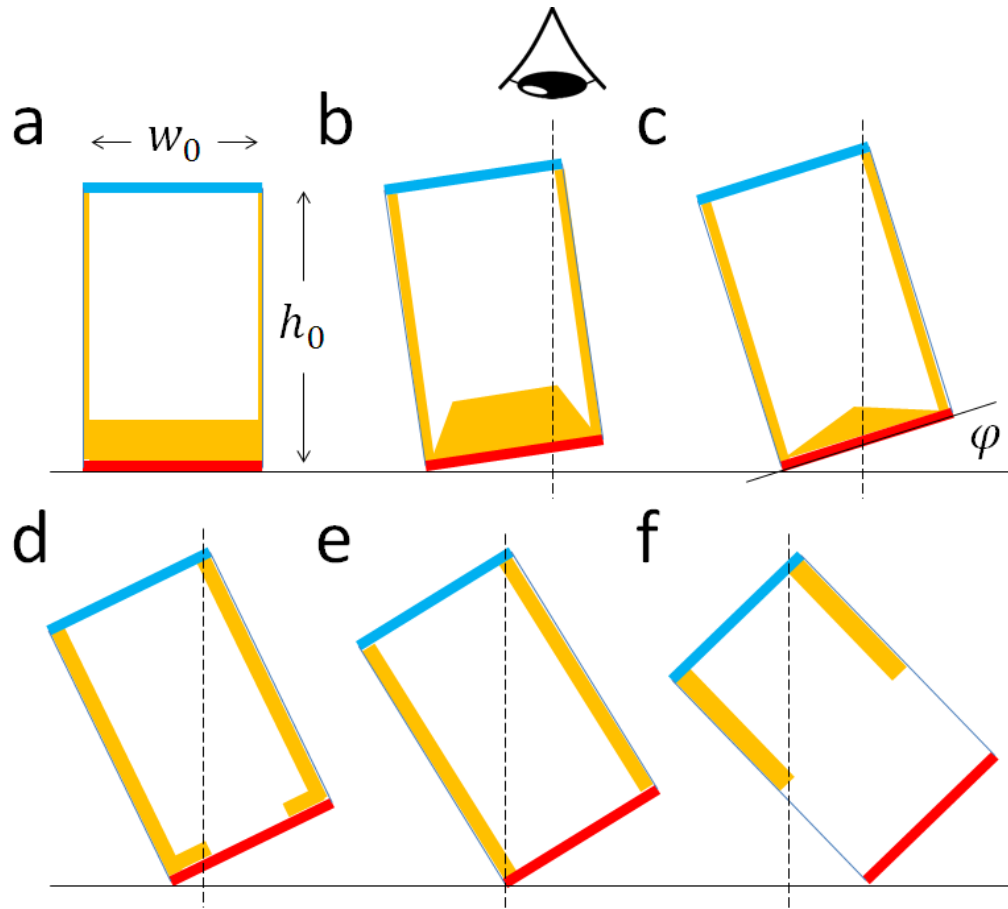


FIG. 2. (Color online) A schematic stick diagram showing the effect of tilt angle  $\varphi$  on the deposition of matter using rotated evaporation via a cylindrical mask. (a) Tilt angle  $\varphi = 0^\circ$ , and (b) to (f) for tilt angles  $\varphi > 0^\circ$ . The mask has dimensions height  $h_0$  and width  $w_0$ . The top (blue) and bottom (red) of the mask can be seen from a bird's-eye view in Fig. 3.

The mask dimensions are an opening width  $w_0$  and height  $h_0$  above the wafer surface. The aspect ratio is thus equal to  $h_0/w_0$ . Intuitively, as the deposition tilt angle  $\varphi$  increases the resulting topography of the material deposition will change. At small values of  $\varphi$  one expects the appearance of well-known flat mesas with little sidewall deposition—Fig. 2(a). At intermediated angles one expects uneven mesa structures on the wafer surface and some sidewall deposition—Figs. 2(b) and (c). At larger angles one expects mainly sidewall deposition with little [Fig. 2(d)] or no [Fig. 2(e)] deposition on the wafer surface. Increasing the tilt further increases sidewall thickness with a lower portion of the sidewall being shadowed by the masking—Figs. 2(f).

The stick diagrams in Fig. 2—where the resist is effectively transparent to us—allow one to have bird's-eye view of what is going on during the deposition and see the top and bottom of the opening simultaneously as seen from the point-of-view of the evaporation source—this is shown in Fig. 3. Note that the particular case-in-point here that of Fig. 2(c).

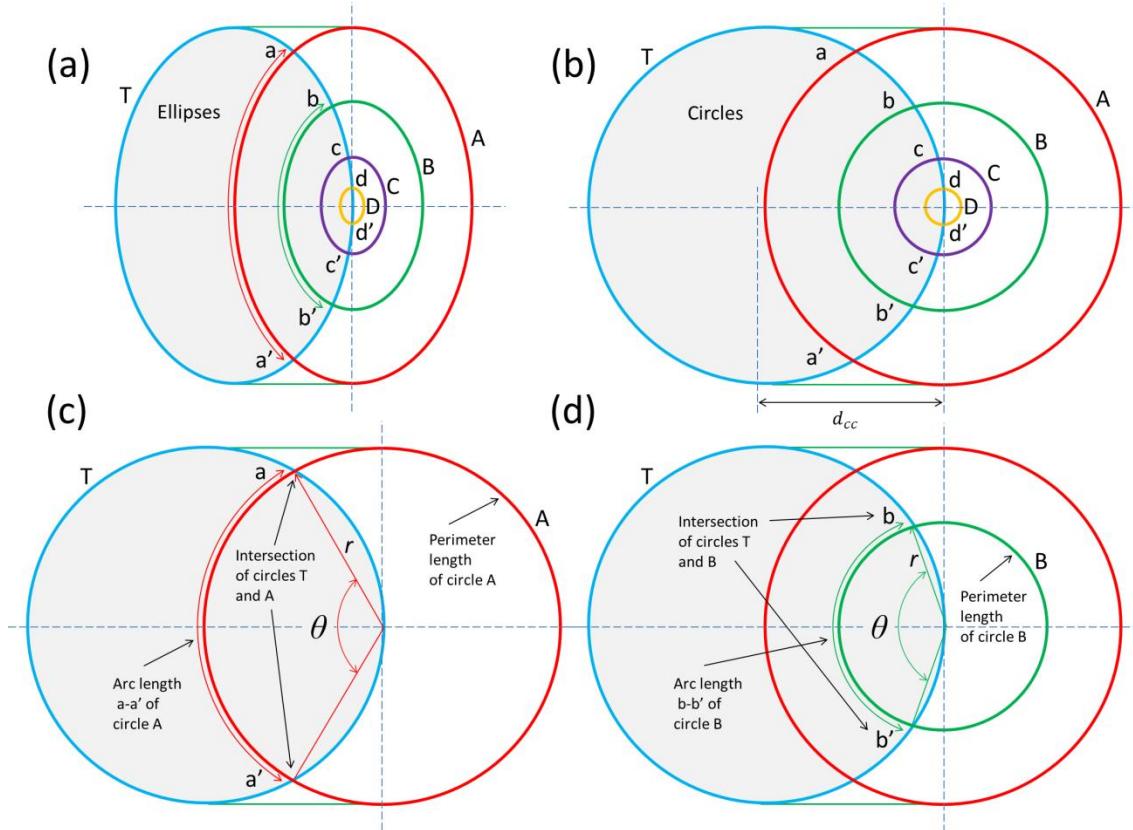


FIG. 3. (Color online) A bird's-eye view of the tilted, rotating evaporation using a circular or cylindrical shaped mask. (a) Ellipses and (b) circles. (c) and (d) show arc lengths to be calculated as  $r$  is varied. The variable  $r$  is the length across the wafer surface. The blue ellipse/circle indicates the top of the mask—the other ellipse/circles (red, green, purple, and yellow) lie on the wafer surface and indicate different values of  $r$ . The case here corresponds to the tilt angle shown Fig. 2(c).

In reality, one would observe tilted circles, i.e. ellipses—see Fig. 3(a), whose eccentricity would depend on the tilt angle. If we consider tilted concentric circles on the bottom of the opening, i.e. the wafer surface; then as the tilted opening rotates, each point lying on an ellipse is deposited with matter when it is *not* in the shadow of the mask.

However, when the point passes into the shadow of the mask, deposition at that point ceases. Thus, in order to calculate the amount of matter which is deposited at that point, one needs to calculate the ratio of an arc of an ellipse to the perimeter of the ellipse as  $r$  is varied. The length of the arc of the ellipse is given by the intersection points with the top ellipse  $T$ . For example, if we consider ellipse  $A$  intersecting ellipse  $T$  in Fig. 3(a)—in order to calculate the thickness of deposited matter along ellipse  $A$  we need to calculate the length of the arc  $a - a'$  and divide by the length of the perimeter of ellipse  $A$ . Likewise, in order to obtain the amount of matter along the perimeter of ellipse  $B$ —one has to calculate the length of the arc  $b - b'$  where ellipse  $B$  intersects ellipse  $T$  and divide this by the length of the perimeter of ellipse  $B$ . It is easy to see that by calculating the amount of matter as a function of the ellipse size one can obtain the profile of the deposited material at the bottom of the opening.

In order to obtain an analytical solution to the problem, the ellipses can be approximated by circles. The error introduced by this approximation can be evaluated by comparing the arc length/perimeter ratio for ellipses of differing eccentricity to that of circles—the latter calculation being trivial. In order to calculate the perimeter of an ellipse an approximation<sup>41</sup> can be used—whereas the arc length of an elliptical sector has to be computed numerically.<sup>42</sup> The following Table gives the percentage error in the arc length/perimeter when using circles rather than ellipses. This error is computed as a function of tilt angle  $\varphi$  and sector angle  $\theta$ .

		Evaporation tilt angle $\varphi$				
Sector angle $\theta$	5°	15°	25°	35°	45°	
10°	99.8%	98.3%	95.1%	89.9%	82.3%	
80°	99.9%	98.8%	96.5%	92.8%	87.2%	

Table: Percentage error comparing the *arc length/perimeter* ratio of circles to that of ellipses as a function of evaporation tilt angle  $\varphi$  and geometric sector angle  $\theta$  (see Fig. 3).

It can be seen that at a tilt angle of  $25^\circ$ , the largest tilt used here, the maximum error of the arc length/perimeter calculation introduced when employing an approximate circular model is  $<5\%$ . As an aside, for a given sector angle  $\theta$ , it is found that the error increases virtually linearly with the square of the tilt angle  $\varphi$ . Finally, one can suggest that a full numerical solution based on the ellipses is possible—but beyond the scope of the work presented here.

We can thus confidently derive a solution using arcs and perimeters of intersecting circles without introducing a large error. We are going to calculate the amount of matter received by each point along the perimeter of a circle—as shown in Fig. 3(b). In the case of a stencil-type mask [Fig. 1(a)], note that the red circles in Figs. 3(c) and 3(d) are not the largest circles that need to be taken into account (see below). At this point the importance of the variable  $r$  should be stated— $r$  is the distance along the wafer surface.

First, we can consider the intersecting circles shown in Fig. 3(c) and Fig. 3(d). When the opening is tilted, the lateral distance between the centre of the top circle  $T$  (i.e. the mask opening) and centre of the projection of this circle onto the wafer surface  $d_{cc}$  is given by:

$$d_{cc} = h \tan \varphi \tag{1}$$

Also, for the circular ‘stencil mask’ opening, with no sidewalls, the furthest that the matter will be evaporated along the wafer surface  $d_e$  will be:

$$d_e = h \tan \varphi + \frac{w}{2} \quad (2)$$

Beyond this, the wafer surface will always be in the shadow of the mask as the system rotates. With reference to Figs. 3(c) and 3(d), by using rudimentary trigonometry and geometry it can be shown that the ratio of an arc  $A$  of a circle to its perimeter  $P$  is given by the following formula:

$$\frac{A}{P} = \frac{1}{\pi} \cos^{-1} \left[ \frac{4h^2 \tan^2 \varphi + 4r^2 - w^2}{8hr \tan \varphi} \right] \quad (3)$$

where  $h$  is the height of the circular opening above the surface,  $w$  is the width of the opening,  $\varphi$  is the evaporation tilt angle of the surface and mask. Note that the ‘tilt angle’ is not the common ‘evaporation angle’ often cited in the literature—here, if  $\varphi = 0$  then the evaporation angle is equal to  $90^\circ$ . The arc of the circle of radius  $r$  is defined from where the circle of radius  $w/2$  (i.e. the top or mask circle) intersects that circle at two points. Physically, the length of the arc on circle radius  $r$  between the two points of intersection is the portion of that circle that is *not in the shadow* of the inclined mask as it rotates. The other—longer—complementary arc is the portion of the circle radius  $r$  that *is* in the shadow of the mask at that moment.

Note that the above Eq. (3) contains  $h$  and  $w$  rather than the mask dimensions  $h_0$  and  $w_0$  as talked about above—the reason for this is as follows. During the deposition of the matter, these initial mask dimensions will be modified due to matter depositing onto

the mask itself. In a first approximation, the following linear formulae can be used to model this:

$$w(t) = w_0 - 2k_w t \quad (4)$$

$$h(t) = h_0 + k_h t \quad (5)$$

where  $w_0$  and  $h_0$  are the mask dimensions *prior* to deposition,  $t$  is the thickness of the deposited matter, and  $k_w$  and  $k_h$  correspond to the lateral and vertical matter deposition coefficients. The signs in Eq. (4) and Eq. (5) ensure that  $h$  increases and  $w$  decreases as the evaporation proceeds. These coefficients can vary from zero to unity. However, from the literature it is possible to estimate the value of  $k_w$ , for example in small metallic cone formation—at small tilt angles—the value of  $k_w$  is  $\sim 0.5$ .<sup>43</sup> The value of  $k_h$  is likely to be of the order of unity for relatively small tilt angle deposition.

A subtle point must be understood now concerning material deposition onto the mask itself. In order for the model to give a reliable result at the radial limit of the evaporation on the wafer surface, i.e. where the evaporated feature's thickness tends to zero, the lateral and vertical deposition coefficients must be such that the following inequality is met:  $\tan \varphi \leq k_w/k_h$ . The reason for this is to ensure that the lower edge of the mask is in the shadow of the new upper edge of the mask after a small deposition of metal. For example, in the practical case where  $k_w = 0.5$  and  $k_h = 1$ —the maximum tilt angle allowed by the model is  $\sim 26.5^\circ$ . At larger tilt angles the shadowing will be due to the lower 'edge' of the mask [indicated by the white arrow in Fig. 1(a)] and the upper edge of the mask [indicated by the red arrow in Fig. 1(a)]—this case, when  $\tan \varphi > k_w/k_h$ , is not dealt with in the current model.

Based on the reasoning here and the assumptions given above, we can now write down the equation for the thickness of a small amount of matter  $\Delta t_d$  deposited along the circle radius  $r$  to the thickness of a small amount of matter  $\Delta t_s$  evaporated by the source—now taking into account the shadowing:

$$\frac{\Delta t_d}{\Delta t_s} = \frac{A}{P} \cos \varphi \quad (6)$$

The factor  $\cos \varphi$  takes into account the effect of glancing angle deposition.<sup>44</sup> Combining Eqs. (3)–(6) gives:

$$\Delta t_d(r) = \frac{\Delta t_s \cos \varphi}{\pi} \cos^{-1} \left[ \frac{4(h_0 + k_h \Delta t_s)^2 \tan^2 \varphi + 4r^2 - (w_0 - 2k_w \Delta t_s)^2}{8r(h_0 + k_h \Delta t_s) \tan \varphi} \right] \quad (7)$$

We can now sum to calculate the total amount of deposited matter  $t_d(r)$ :

$$t_d(r) = \sum_{n=1}^{n=N} \frac{\Delta t_s \cos \varphi}{\pi} \cos^{-1} \left[ \frac{4(h_0 + k_h n \Delta t_s)^2 \tan^2 \varphi + 4r^2 - (w_0 - 2k_w n \Delta t_s)^2}{8r(h_0 + k_h n \Delta t_s) \tan \varphi} \right] \quad (8)$$

where:

$$N = \frac{t_s}{\Delta t_s} \quad (9)$$

Despite being a geometric model,  $N$  can be chosen to give an acceptable resolution, e.g. for a thickness of evaporated gold equal to 100 nm choosing  $N = 250$  results in a resolution of  $\sim 0.4$  nm—i.e. of the order of the lattice constant<sup>45</sup> and achievable surface roughness.<sup>46</sup> Thus, in principle experimental results which deviate from the predictions are likely to be due to material issues, e.g. granularity. It is thus a relatively simple task to set up the solution for the deposition at the wafer surface. The total value of  $t_d$  at a given radius  $r$  on the wafer surface can be evaluated by summing all

the values of  $\Delta t_d$  as  $w$  and  $h$  vary according to the lateral and vertical deposition coefficients—this can be performed using a simple array.

#### IV. A MODEL FOR THE TOPOGRAPHY OF MATTER DEPOSITED ONTO THE SIDEWALL

The model for the deposition of matter on the sidewall of a cylindrical mask uses a similar approach and reasoning to that given above. Again, one imagines the bird’s-eyes view of the projection of the tilted, circular opening onto the sidewall of the cylinder—see Fig. 4.

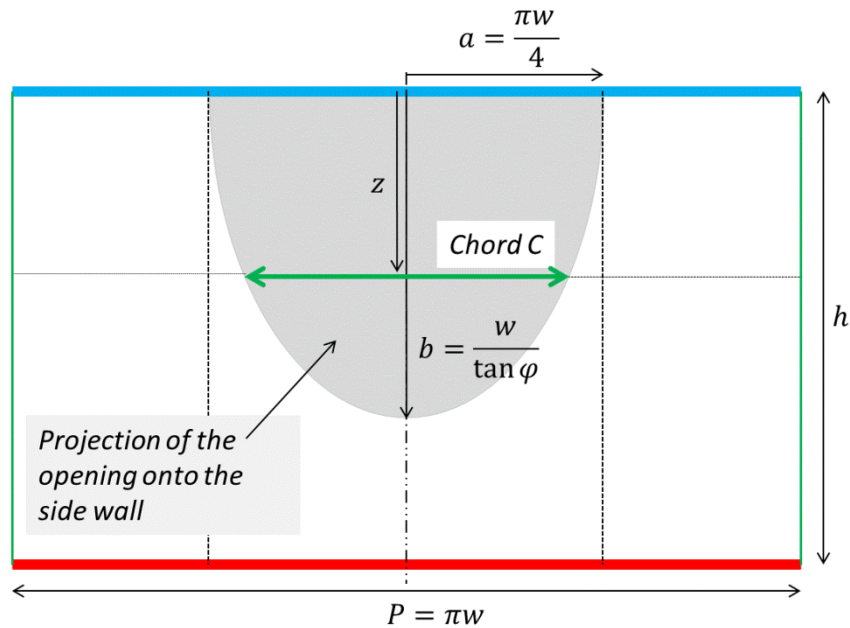


FIG. 4. (Color online) Deposition on the sidewall. The ellipse (shaded grey) is a projection of the circular opening of the mask onto the inside of the cylinder (flattened out in the Figure). The blue and red lines indicate the top and bottom of the cylinder. The projected ellipse has half axes  $a$  and  $b$ —and contains a chord  $C$ . The perimeter  $P$  of the

cylinder is equal to  $\pi w$ . The variable  $z$  is the vertical distance along and down the sidewall of the cylinder.

It important to note that a distinction is made between the calculated sidewall deposition, in practice this would be the walls of the resist profile shadowed by a pre-fabricated resist ‘overhang’ feature, and the deposition on the mask—due to  $k_w$  in the model—which increases shadowing as the deposition proceeds. Indeed, extensive experimental studies, cited above, into the fabrication of sharp points demonstrate that these are apparently not the same—the mask accumulating more deposition in the absence of shadowing than the shadowed sidewalls.

In the case of tilted sidewall deposition, one computes the length of the *chord*  $C$  of the half ellipse resulting from this projection to the circular perimeter  $P$  of the cylinder opening, i.e.  $\pi w$ . This chord is orthogonal to the vertical direction  $z$  of the opening. We can write down the ratio of the chord length  $C$  at  $z$  to the perimeter  $P$  of the inside of the cylinder:

$$\frac{C}{P} = \frac{1}{2} \cos \left[ \sin^{-1} \left( \frac{z \tan \varphi}{w} \right) \right] \quad (10)$$

where  $z$  is the vertical distance down the side of the inside of the cylinder, and the other parameters have their meanings above.

As above, we can write down the equation for the thickness of matter deposited  $\Delta t_d$  along the circle containing the chord—at height  $z$ —to the thickness evaporated by the source  $\Delta t_s$  as:

$$\frac{\Delta t_d}{\Delta t_s} = \frac{C}{P} \sin \varphi \quad (11)$$

Where the factor  $\sin \varphi$  takes into account the glancing angle deposition. Assuming that  $w$  and  $h$  vary as above in Eq. (4) and Eq. (5)—due to deposition on the mask opening—we can combine these with Eq. (10) and Eq. (11) to give:

$$\Delta t_d(z) = \frac{\Delta t_s \sin \varphi}{2} \cos \left[ \sin^{-1} \left( \frac{(z+k_h \Delta t_s) \tan \varphi}{w_0 - 2k_w \Delta t_s} \right) \right] \quad (12)$$

Note that the factor  $z + k_h \Delta t_s$  accounts for the deposition of matter on top of the mask in the case of sidewall deposition—effectively leading to the projected half-ellipse being shifted up as the deposition proceeds. As above, we can now sum to calculate the thickness of the deposited matter on the sidewalls  $t_d(z)$ :

$$t_d(z) = \sum_{n=1}^{n=N} \frac{\Delta t_s \sin \varphi}{2} \cos \left[ \sin^{-1} \left( \frac{(z+k_h n \Delta t_s) \tan \varphi}{w_0 - 2k_w n \Delta t_s} \right) \right] \quad (13)$$

where:

$$N = \frac{t_s}{\Delta t_s} \quad (14)$$

Again, it is a relatively simple task to set up the solution. The total value of  $t_d$  at a given height on the cylinder at  $z$  can be evaluated by summing all the values of  $\Delta t_d$  as  $w$  and  $h$  vary according to the lateral and vertical deposition coefficients—this can also be performed using a simple array. Note in this case that the lateral deposition coefficient applies only to the mask opening as it is not shadowed—as explained above. And let us recall again the condition  $\tan \varphi \leq k_w/k_h$  must be satisfied. Finally, note that in both cases above, the quotient of the inverse trigonometric functions, i.e.  $\cos^{-1}$  or  $\sin^{-1}$ , in Eq.

(8) and Eq. (13) needs to be checked to be in the range  $\pm 1$ . If they fall outside this value, the physical interpretation of this is that either there is no shadowing during rotation or total shadowing.

## **V. SOME PRACTICAL PREDICTIONS OF THE MODEL**

Figs. 5 and 6 show some predictions of the modelling when changing the tilt angle  $\varphi$  and the aspect ratio  $h_0/w_0$  of the masking.

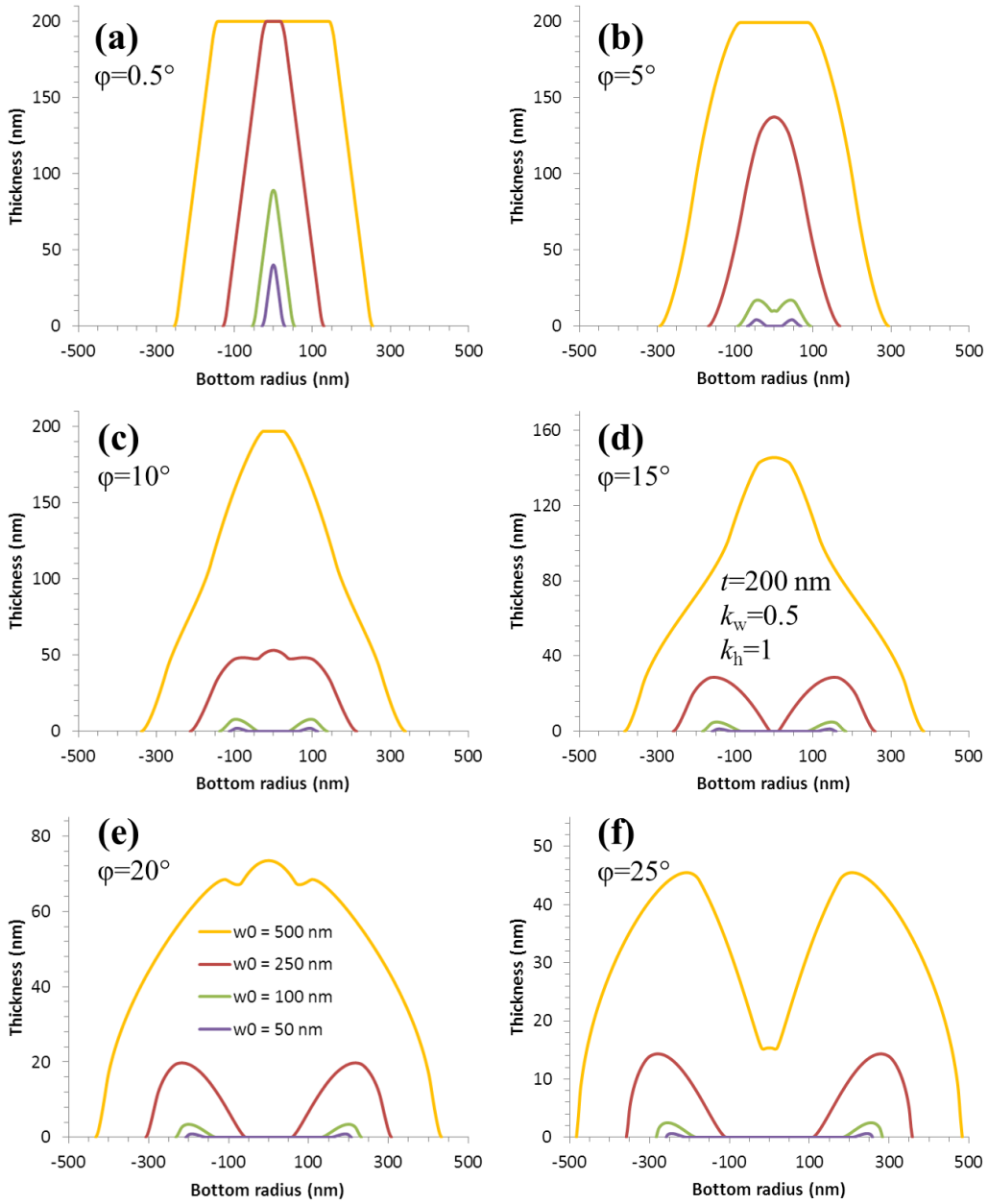


FIG. 5. (Color online) Cross-sectional topography of deposited matter on the wafer surface for a stencil mask as a function of tilt angle and mask opening. The deposition tilt angle  $\varphi$  is (a)  $0.5^\circ$ , (b)  $5^\circ$ , (c)  $10^\circ$ , (d)  $15^\circ$ , (e)  $20^\circ$ , and (f)  $25^\circ$ . At each tilt angle the masking aspect ratio  $h_0/w_0$  is 1 (gold curves), 2 (violet curves), 5 (green curves), and 10

(blue curves). Total evaporated matter thickness  $t = 200\text{nm}$  and the deposition coefficients  $k_w$  and  $k_h$  are 0.5 and 1 respectively.  $h_0 = 500\text{ nm}$ .

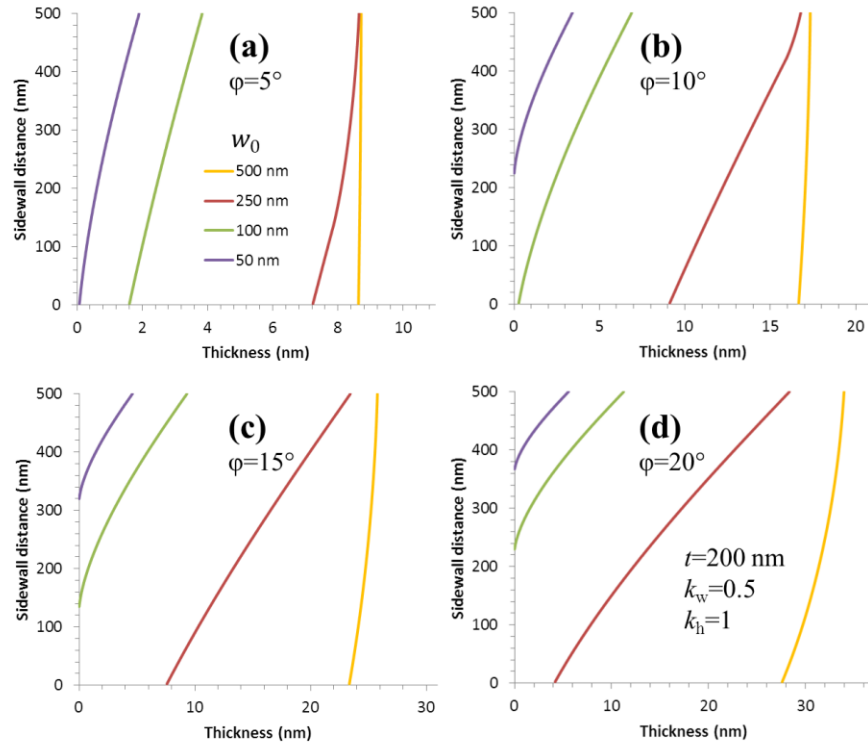


FIG. 6. (Color online) Cross-sectional topography of deposited matter on the sidewall of a cylindrical mask as a function of tilt angle and mask opening. The deposition tilt angle  $\varphi$  is (a)  $5^\circ$ , (b)  $10^\circ$ , (c)  $15^\circ$ , and (d)  $20^\circ$ . At each tilt angle the masking aspect ratio  $h_0/w_0$  is 1 (gold curves), 2 (violet curves), 5 (green curves), and 10 (blue curves). Total evaporated matter thickness  $t = 200\text{nm}$  and the deposition coefficients  $k_w$  and  $k_h$  are 0.5 and 1 respectively.  $h_0 = 500\text{ nm}$ .

In order to produce these plots some realistic practical numbers have been used. First, the mask dimensions have been chosen to reflect those commonly used in electron

beam (ebeam) lithographic processes. The value of  $h_0$  is 500 nm and the values of  $w_0$  is varied from 50 nm to 500 nm—i.e. an aspect ratio ( $h_0/w_0$ ) varying from 10 down to 1. The values of  $k_w$  and  $k_h$  are taken to be 0.5 and 1—it should be noted that these parameters are likely to be depended on the tilt angle, but this is not considered in the current approximation. The values of  $k_w$  and  $k_h$  imply that the maximum tilt angle is about  $26.5^\circ$ . A deposition thickness of 200 nm is used. Fig. 5 plots the mesa topography using a circular stencil mask [see Fig. 1(a)] whilst Fig. 6 plots the expected sidewall deposition using a cylindrical mask [see Fig. 1(b)].

Let us first consider Fig. 5. First, in the case of small tilt angle and large aspect ratio [Fig. 5(a)] we find square-cornered mesa structures (gold curve). As the aspect ratio is increased, we see the appearance of small cone-like structures (green and blue curves)—the height of the cones decreasing with increasing aspect ratio. As the deposition tilt angle is gradually increased [Fig. 5(b) to Fig. 5(f)] interesting mesa topographies become apparent. At a tilt angle of  $5^\circ$  [Fig. 5(b)] and a relatively large aspect ratio ( $h_0/w_0 = 5$ ), a mesa having a dip in the centre appears [green curve in Fig. 5(b)]. Increasing the aspect ratio to 10 results in the formation of a ring-like structure resembling a cut bagel. At a tilt angle equal to  $10^\circ$  [Fig. 5(c)], an aspect ratio of unity results in a large quasi-conic structure [gold curve in Fig. 5(c)]. Increasing the aspect ratio leads to the formation of a mesa having a small ‘bump’ in the centre [violet curve in Fig. 5(c)], followed by ring-like structures at higher aspect ratio [green and blue curves in Fig. 5(c)]. At a tilt angle of  $15^\circ$  [Fig. 5(d)] and an aspect ratio of unity (gold curve) a large, more pointed mesa structure is expected. At higher aspect ratios ring formation begins at lower aspect ratio—with thicker ‘half-bagel’ rings being formed. At the two

highest tilt angles [Fig. 5(e) and 5(f)] very different mesa structures are predicted at unity aspect ratio to that when the tilt angle tends to zero. Here we find an irregular bump [gold curve in Fig. 5(e)] and a ring-like structure which is not open [gold curve in Fig. 5(f)]. Increasing the aspect ratio in both cases leads to ring formation—wider rings being formed at higher tilt angles.

Fig. 6 show the predictions of the model concerning sidewall deposition when using a cylindrical mask as described in Fig. 1(b). When the tilt angle is low ( $\varphi < 5^\circ$ ), there is a very thin uniform film deposited over the whole of the sidewall. This film thickness corresponds to  $< 1$  nm for an evaporation of 200 nm (not shown here). As the tilt angle is increased beyond  $5^\circ$  the film thickness becomes greater and deposition uniformity remains relatively constant for small aspect ratios (gold curves). At the two higher tilt angles [Figs. 6(c) and 6(d)] the sidewall deposition at unity aspect ratio starts to become non-uniform—but is still present over the whole of the sidewall. As we increase the aspect ratio of the mask and increase the tilt angle two effects become apparent. First, the sidewall film thickness become non-uniform, and second, in some cases the film does not extend to the bottom of the sidewall. For example, at a tilt angle of  $20^\circ$  [Fig. 6(d)] and an aspect ratio of 5 (brown curve), the film thickness varies from 28 nm down to 4 nm in a relatively linear fashion. However, at larger aspect ratios, i.e. when  $\varphi > \varphi_c$  where  $\varphi_c = \tan^{-1} w_0/h_0$ —this is a critical tilt angle, there is no sidewall deposition over the whole of the side. In this case the sidewall deposition would form cylindrical structures of a non-uniform thickness on the sidewalls of the cylindrical mask—see larger aspect ratios in Figs. 6(b) to 6(d). On a practical note, at the larger tilt angles the film thickness becomes a non-negligible proportion of the evaporated matter

thickness  $\sim 20\%$ . Up to the critical tilt angle  $\varphi_c$ , this film—depending on its mechanical robustness—may ‘survive’ the *lift-off* process and form a cylinder/mesa feature. It should be noted that if—for whatever reason—a liquid suspension of solid cylindrical features of certain dimensions were required, then rotated evaporation using a large tilt angle and a large aspect ratio—followed by a *lift-off* process—would enable this practically.

Now let us investigate how the model predicts the formation of cones (Fig. 7), spikes (Fig. 8), and rings (Fig. 9).

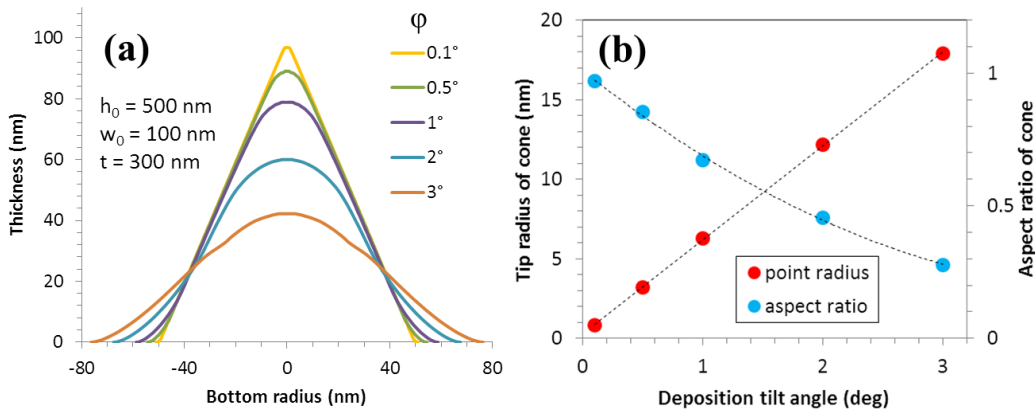


FIG. 7. (Color online) Cone formation at small deposition angles. (a) An example of the evolution of a cone’s topography as a function of deposition angle  $\varphi$  from  $0.1^\circ$  to  $3^\circ$ . The aspect ratio ( $h_0/w_0$ ) of the masking is 5, and the total deposited material thickness is 300 nm. (b) The variation of the cone’s tip radius of curvature (red circles) and the aspect ratio of the cone (*height/base width*)—blue circles. The values of the deposition coefficients  $k_w$  and  $k_h$  are equal to 0.5 and 1 respectively.

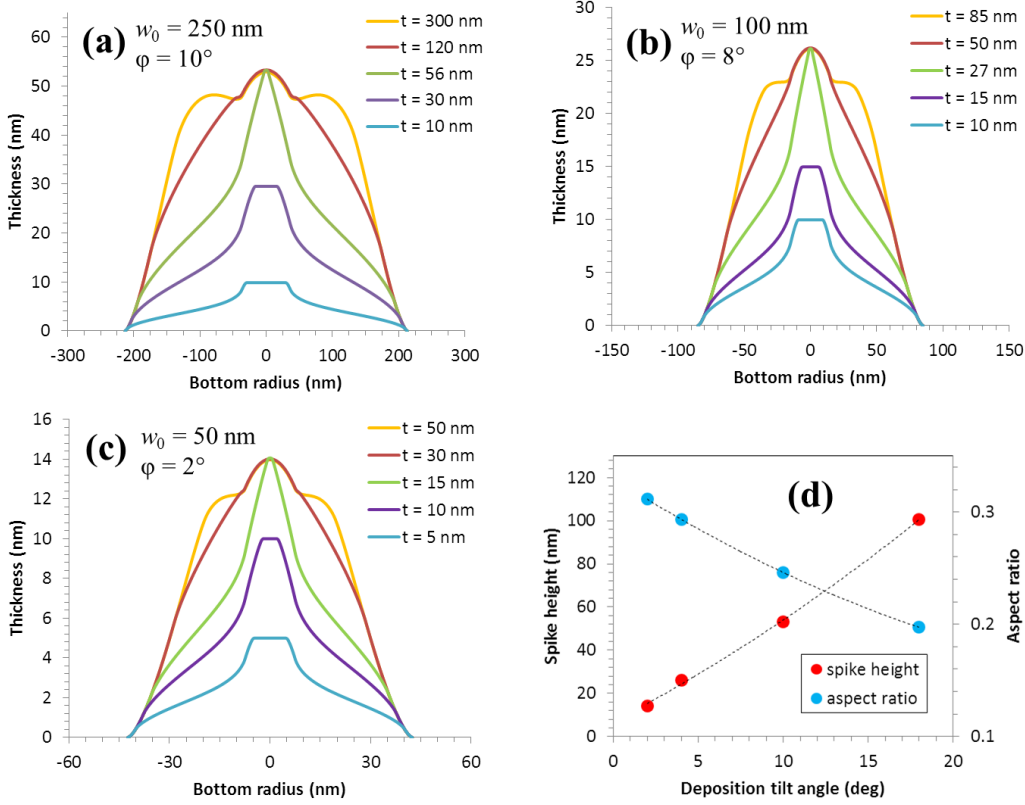


FIG. 8. (Color online) Spike formation as a function of total deposited matter thickness  $t_s$ . For (a) a deposition angle  $\varphi = 10^\circ$  and an aspect ratio  $h_0/w_0 = 2$ , (b) a deposition angle  $\varphi = 8^\circ$  and an aspect ratio  $h_0/w_0 = 5$ , and (c) a deposition angle  $\varphi = 2^\circ$  and an aspect ratio  $h_0/w_0 = 10$ . (d) A plot of the calculated spike height (red circles) and the spike aspect ratio—spike height/spike base width—(blue circles). The values of the deposition coefficients  $k_w$  and  $k_h$  are equal to 0.5 and 1 respectively.

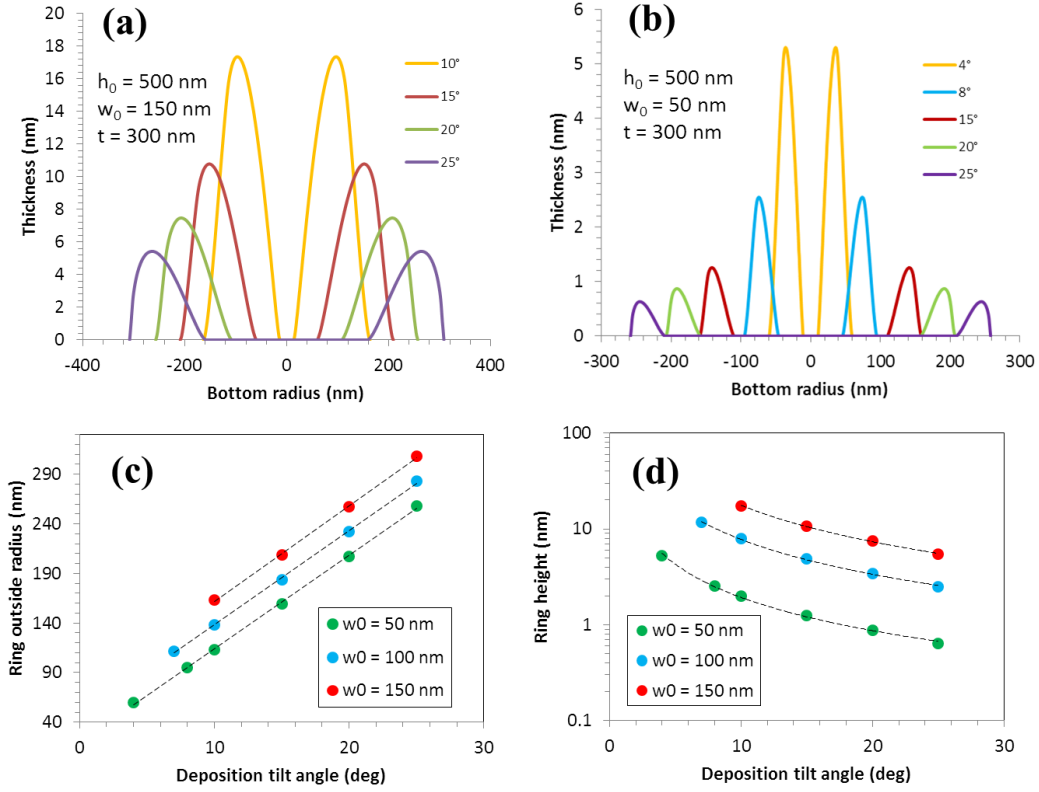


FIG. 9. (Color online) Ring formation at large deposition angles. (a) the evolution of rings topography as a function of deposition angle  $\phi$  from  $10^\circ$  to  $25^\circ$ . The aspect ratio ( $h_0/w_0$ ) of the masking is 3.3, and the total deposited material thickness is 300 nm. (b) the evolution of rings topography as a function of deposition angle  $\phi$  from  $4^\circ$  to  $25^\circ$ . The aspect ratio ( $h_0/w_0$ ) of the masking is 1, and the total deposited material thickness is 300 nm. (c) Variation of the ring's outside radius as a function of tilt angle and masking aspect ratio. (d) Variation of the ring's maximum height as a function of tilt angle and masking aspect ratio.

First, in terms of cone-like feature formation [Fig.7(a)], it can be seen that increasing the tilt angle increases the radius of curvature of the tip of the cone [Fig.

7(b)]—the tip radius increasing approximately linearly with tilt angle. The aspect ratio of the cone decreases with increasing tilt angle. Fig. 8 shows the formation of ‘spikes’ sitting on a flat mesa. For a given tilt angle  $\varphi$  and masking aspect ratio  $h_0/w_0$  a sharp spike appears at a critical deposition thickness  $t_c$ —green curves in Figs. 8(a)–(c). If  $t > t_c$  bumps are formed (gold curves), if  $t < t_c$  then flat-topped mesa structures are formed (blue curves). The aspect ratio of the spike is largest at lower tilt angle—see Fig. 8(d). Fig. 9 shows the effect of tilt angle and masking aspect ratio on the formation of ‘bagel’ type rings. First, it can be seen that the tilt angle  $\varphi$ , the masking aspect ratio  $h_0/w_0$ , and the deposited thickness  $t$  can be set to determine a unique bagel-type ring structure having a well-defined inner and outer radius, and a maximum ring thickness. The ring width is equal to  $w_0$ , and the ring outer radius is equal to  $h_0 \tan \varphi + w_0/2$ . The maximum ring height  $h_{max}$ , which diminishes with increasing tilt angle  $\varphi$  and increasing masking aspect ratio  $h_0/w_0$ , must be calculated from the model follow a power law.

Finally, Fig. 10 shows a summary of some of the topographies which are predicted using the model.

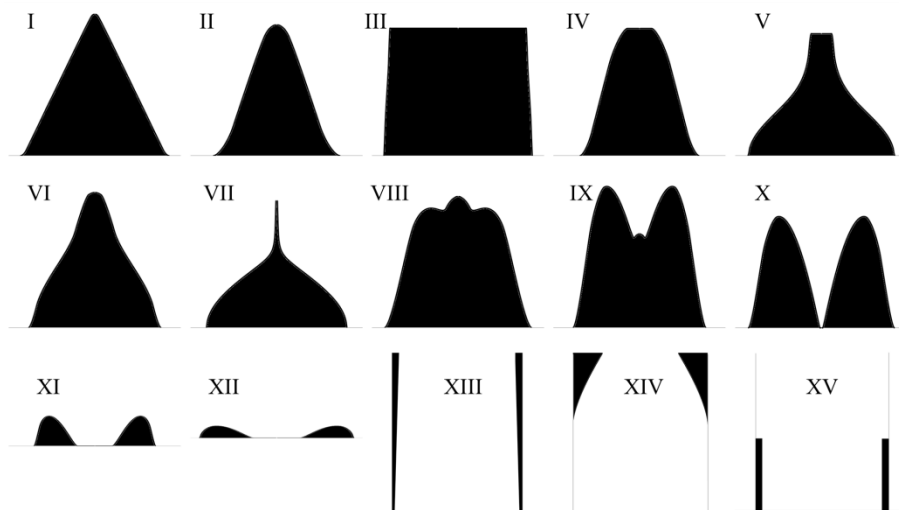


FIG. 10. A schematic diagram showing some of the topologies (cross-section) predicted by the modelling. (i) sharp-tipped cones, (ii) round-tipped ‘blunt’ cones, (iii) square mesa, (iv) flat-topped mesa, (v) bottle-necked mesa, (vi) rounded mesa, (vii) spiked-mesa, (viii) bump type 1, (ix) bump type 2, (x) closed-centre ring (xi) thick ‘half bagel-type’ ring, (xii) flat ring, (xiii) tall thin cylinder connected to the wafer surface, (xiv) a short thick cylinder not connected to the wafer surface, and (xv) a short uniform-thickness cylinder attached to the wafer surface.

One can identify at least 15 distant forms which could—in principle—be fabricated on the sub-micrometre scale using tilted rotated evaporation via an ebeam mask. The identified topologies are (i) sharp-tipped cones, (ii) round-tipped ‘blunt’ cones, (iii) square mesa, (iv) flat-topped mesa, (v) bottle-necked mesa, (vi) rounded mesa, (vii) spiked-mesa, (viii) bump type 1, (ix) bump type 2, (x) closed-centre ring (xi) thick ‘half bagel-type’ ring, and (xii) flat ring, (xiii) tall thin cylinder connected to the wafer surface, (xiv) a short thick cylinder not connected to the wafer surface, and (xv) a short uniform-thickness cylinder attached to the wafer surface. Inclined rotating evaporation via a mask under the conditions given in the paper should result in nanostructure forms resembling these.

## **VI. Application of the ideas to an idealized circular ‘resist-based’ *lift-off* mask**

By extending the above ideas it is possible to develop a model for deposition using an ‘idealized circular *lift-off* mask’—shown in Fig. 11. Despite being an approximation of a ‘real’ resist *lift-off* profile—it should, at least in principle, be of help to the process engineer to enable him or her to predict structuration resulting from inclined rotated evaporation using a practical mask. Fig. 11(a) shows the idealized circular resist-based *lift-off* mask considered here.

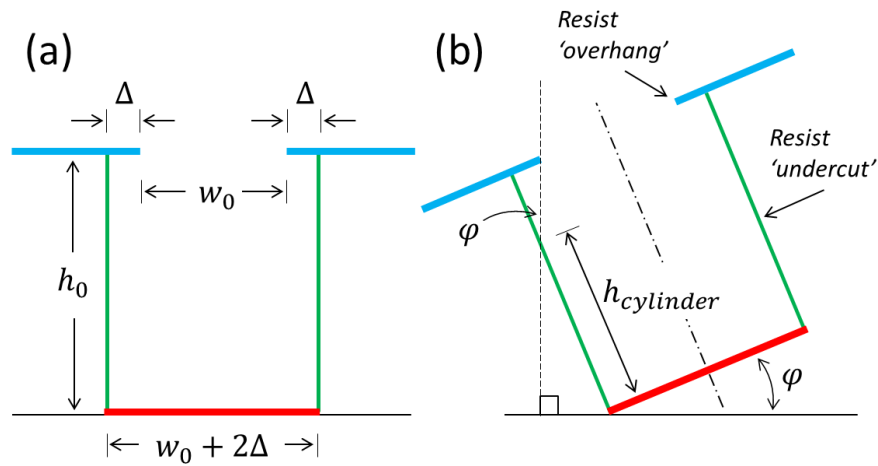


FIG. 11. (Color online) A schematic diagram of an idealized circular *lift-off* mask at (a)  $\varphi = 0^\circ$  showing relevant dimension, and inclined (b) where  $\varphi > 0^\circ$ . The overhang features (blue) have length  $\Delta$  and are considered infinitely thin, meaning that the undercut sidewalls (green) width is  $w_0 + 2\Delta$  and its height is  $h_0$ . Depending on the dimensions and the tilt angle  $\varphi$ , the deposition can occur on the wafer surface (red) and on the undercut sidewalls (green). The dashed black line in (b) indicates the axis of rotation during deposition.

The two main features of such as mask are the well-known ‘*overhang*’ and an ‘*undercut*’. These features are there for good reason—to , and in practice are achieved either by surface modification prior to resist development<sup>14,15</sup>—the latter often emphasized, or using single<sup>16</sup> or bilayers<sup>47</sup> where resist solubility in the vertical direction is modified by ebeam exposure. Such lift-off masks can have sub-10 nm openings.

In the idealized theoretical case here, the overhang feature has a length equal to  $\Delta$  and zero width. The undercut sidewalls are considered to be vertical, having height  $h_0$ . The resist mask opening is  $w_0$ —meaning that the width of the undercut is  $w_0 + 2\Delta$  [see Fig.11(a)]. When this mask is inclined for evaporation there are two points to note which differ from the cases discussed above. First, as the undercut features extend to the bottom of the wafer the deposition *on the wafer surface* stops at  $w_0/2 + \Delta$ . Thus, for this idealized *lift-off* mask Eq. (8) can be used by truncating deposition beyond the limit  $r > w_0/2 + \Delta$  on the wafer surface.

An approximate solution for the sidewall deposition when overhang features are involved can be explained using Fig. 12.

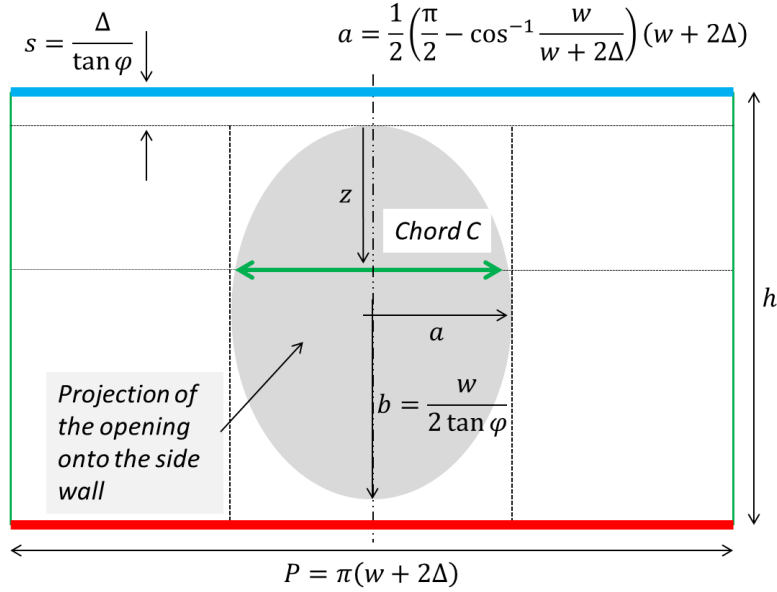


FIG. 12. (Color online) Deposition on the sidewalls when using an idealized *lift-off* mask. The ellipse (shaded grey) is a projection of the circular opening of the mask onto the inside of the cylinder (flattened out in the Figure). The blue and red lines indicate the top and bottom of the cylinder. The projected ellipse has half axes  $a$  and  $b$ —and contains a chord  $C$ . The perimeter  $P$  of the cylinder is equal to  $\pi(w + 2\Delta)$ . A masked region exists which is shadowed by the overhangs—this has a width  $s$  of  $\Delta/\tan \varphi$ .

Fig. 12 shows the lengths of the half axes  $a$  and  $b$  of the projected ellipse of the opening in the presence of the overhang feature. When an overhang feature is present, the projection of the opening will be a full ellipse onto the sidewall of the resist profile—*cf.* Fig. 4. With reference to Fig. 12, again by using basic trigonometry it can be shown that the ratio of the chord  $C$  to the perimeter  $P$  is given by:

$$\frac{C}{P} = \frac{1}{\pi} \left[ \frac{\pi}{2} - \cos^{-1} \left( \frac{w}{w+2\Delta} \right) \right] \cos \left[ \sin^{-1} \left( \frac{2z \tan \varphi}{w} \right) \right] \quad (15)$$

Following the same steps as above, we can now write down the approximate expression for the deposition on the sidewall  $t_d(z)$  as:

$$t_d(z) = \sum_{n=1}^N \frac{\Delta t_s \sin \varphi}{\pi} \left[ \frac{\pi}{2} - \cos^{-1} \left( \frac{w_0 - 2k_w n \Delta t_s}{w_0 - 2(k_w n \Delta t_s - \Delta)} \right) \right] \cos \left[ \sin^{-1} \left( \frac{2(z + k_h n \Delta t_s) \tan \varphi}{w_0 - 2k_w n \Delta t_s} \right) \right] \quad (16)$$

where the symbols have the same meaning as above.

Although being an idealized *lift-off* resist profile, by using some reasonable practical values used currently in ebeam processing<sup>18</sup> one can make some predictions using truncated Eq. (8) and Eq. (16). Let us take the overhang length  $\Delta$  to be 25 nm, the resist height  $h_0$  to be 300 nm, and the resist opening  $w_0$  to be 100 nm. Let the total evaporated thickness  $t_s$  be 300 nm. The predicted nanostructuration on the wafer surface and on the undercut sidewalls can be plotted as a function of deposition tilt angle  $\varphi$ —this is shown in Fig. 13.

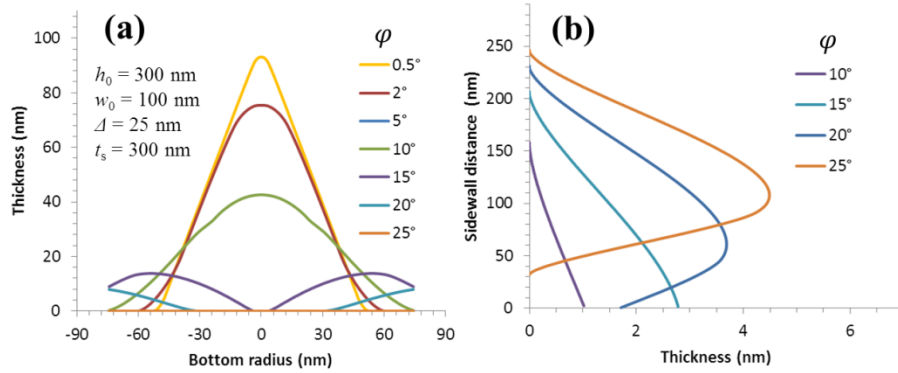


FIG. 13. (Color online) Plots of the predicted nanostructuration topography using the idealized circular resist-based *lift-off* model. (a) Deposition on the wafer surface. (b) Deposition on the undercut sidewalls. The deposition tilt angle  $\varphi$  is varied from 0.5° to

25°. The values of the deposition coefficients  $k_w$  and  $k_h$  are equal to 0.5 and 0.5 respectively.

First, considering Fig. 13(a) one can still observe the evolution of the deposition on the wafer surface from conic mesa structures (gold, brown and green) to rings (violet and light blue). Second, considering Fig. 13(b) one can observe the influence of the overhang feature on the deposition. First, small flat cylinders will be formed at a low tilt angles ( $<10^\circ$ —not shown)—indeed, cylinder formation begins at a critical angle  $\varphi = \tan^{-1} \Delta/h_0$ —about  $4.8^\circ$  here. From  $\varphi = 10^\circ$  thicker, taller cylinders are formed (violet, light blue, and dark blue curves) which become thicker and less uniform as the tilt angle is increased. Above a critical angle  $\varphi = \tan^{-1} w_0 + \Delta/h_0$ , the cylinders deposited onto the sidewall become detached from the surface (light brown curve). In principle—at least—cylinder formation continues up to  $\varphi = 90^\circ$ , with thicker narrow bands being formed. The height of the cylinders which are attached to the surface is given by 
$$h_{cylinder} = h_0 - \Delta/\tan \varphi.$$

## VII. SUMMARY AND CONCLUSIONS

Using some approximations and assumptions a simple analytical model can be derived which can be used to predict the shape of a small material feature resulting from the rotating inclined evaporation process using small circular and cylindrical openings obtained using a typical microelectronics resist on a flat wafer surface. Both the material topography of the resulting mesa on the wafer surface, and the deposition on the sidewalls of a cylindrical-shaped opening mask, can be predicted using the model. The

predictions of the modelling are extensive. Depending on whether the mask is circular or cylindrical, of high aspect ratio, a high tilt angle, and the total evaporated matter—the resulting material topography can be in the form of sharp-tipped cones, round-tipped cones, spikes, bumps, flat-topped mesas, bagel-shaped rings, flat rings, and vertical cylinders attached to the surface/or mesa or free-standing. The ideas are extended to model an idealized ‘resist-based’ *lift-off* mask comprising overhang features and an undercut—this should be useful for the process engineer as it approximates a practical resist profile. Despite its simplicity, and being an approximation, the model should help to understand the sensitivity of the final topography of the PVD deposited matter on the various parameters. Thus, the prediction—and indeed optimization—of the shape of deposited material in a small mask opening is possible prior to embarking on time-consuming, and perhaps costly, extensive experimentation.

## ACKNOWLEDGEMENTS

The author acknowledges financial support from the French *Agence Nationale de La Recherche* (ANR) funded ‘TIPTOP\_1’ project (ANR-16-CE09-0029) and the French *Hauts-de-France* region funded projects (DOS0025370/00 and 17007720). The author would very much like to thank both Thomas and Rose Arscott for fruitful discussions that helped me visualize the problem.

<sup>1</sup> M.M. Hawkeye and M.J. Brett, *J. Vac. Sci. Technol. Vac. Surf. Films* **25**, 1317 (2007).

<sup>2</sup> M.J. Madou, *Fundamentals of Microfabrication: The Science of Miniaturization, Second Edition* (CRC Press, 2002).

<sup>3</sup> S. Kubatkin, A. Danilov, M. Hjort, J. Cornil, J.-L. Brédas, N. Stuhr-Hansen, P. Hedegård, and T. Bjørnholm, *Nature* **425**, 698 (2003).

- <sup>4</sup> S. Franssila, *Introduction to Microfabrication: Franssila/Introduction to Microfabrication* (John Wiley & Sons, Ltd, Chichester, UK, 2010).
- <sup>5</sup> D.H. Tien, J.-Y. Park, K.B. Kim, N. Lee, and Y. Seo, *Sci. Rep.* **6**, (2016).
- <sup>6</sup> C.A. Spindt, *J. Appl. Phys.* **39**, 3504 (1968).
- <sup>7</sup> C.A. Spindt, I. Brodie, L. Humphrey, and E.R. Westerberg, *J. Appl. Phys.* **47**, 5248 (1976).
- <sup>8</sup> A.J. Melmed, *J. Vac. Sci. Technol. B Microelectron. Nanometer Struct.* **9**, 601 (1991).
- <sup>9</sup> J.M. Kontio, H. Husu, J. Simonen, M.J. Huttunen, J. Tommila, M. Pessa, and M. Kauranen, *Opt. Lett.* **34**, 1979 (2009).
- <sup>10</sup> G. Dolling, M. Wegener, and S. Linden, *Opt. Lett.* **32**, 551 (2007).
- <sup>11</sup> N. Liu, H. Guo, L. Fu, S. Kaiser, H. Schweizer, and H. Giessen, *Nat. Mater.* **7**, 31 (2007).
- <sup>12</sup> P.K. Jain and M.A. El-Sayed, *Chem. Phys. Lett.* **487**, 153 (2010).
- <sup>13</sup> A. Nemiroski, M. Gonidec, J.M. Fox, P. Jean-Remy, E. Turnage, and G.M. Whitesides, *ACS Nano* **8**, 11061 (2014).
- <sup>14</sup> G.J. Dolan, *Appl. Phys. Lett.* **31**, 337 (1977).
- <sup>15</sup> M. Hatzakis, B.J. Canavello, and J.M. Shaw, *IBM J. Res. Dev.* **24**, 452 (1980).
- <sup>16</sup> W. Chen, *J. Vac. Sci. Technol. B Microelectron. Nanometer Struct.* **11**, 2519 (1993).
- <sup>17</sup> C. Vieu, F. Carcenac, A. Pépin, Y. Chen, M. Mejias, A. Lebib, L. Manin-Ferlazzo, L. Couraud, and H. Launois, *Appl. Surf. Sci.* **164**, 111 (2000).
- <sup>18</sup> Y. Chen, *Microelectron. Eng.* **135**, 57 (2015).
- <sup>19</sup> J.M. Bennett and E.J. Ashley, *Appl. Opt.* **12**, 758 (1973).
- <sup>20</sup> M. Gross, S. Dligatch, and A. Chtanov, *Appl. Opt.* **50**, C316 (2011).
- <sup>21</sup> S.M. Rossnagel, *J. Vac. Sci. Technol. B Microelectron. Nanometer Struct.* **16**, 2585 (1998).
- <sup>22</sup> S.M. Sze, editor, *VLSI Technology. Hauptband: ..., 2. ed* (McGraw-Hill, New York, 1988).
- <sup>23</sup> W.G. Oldham, A.R. Neureuther, Chiakang Sung, J.L. Reynolds, and S.N. Nandgaonkar, *IEEE Trans. Electron Devices* **27**, 1455 (1980).
- <sup>24</sup> W. Colquhoun, R. Sokol, E. Davison, and L. Cassimeris, *J. Electron Microsc. Tech.* **2**, 353 (1985).
- <sup>25</sup> W. Colquhoun and R. Sokol, *J. Electron Microsc. Tech.* **3**, 169 (1986).
- <sup>26</sup> E.W. Scheckler and A.R. Neureuther, *IEEE Trans. Comput.-Aided Des. Integr. Circuits Syst.* **13**, 219 (1994).
- <sup>27</sup> M. Fujinaga and N. Kotani, *IEEE Trans. Electron Devices* **44**, 226 (1997).
- <sup>28</sup> D. Vick, L.J. Friedrich, S.K. Dew, M.J. Brett, K. Robbie, M. Seto, and T. Smy, *Thin Solid Films* **339**, 88 (1999).
- <sup>29</sup> M. Lishchynska, V. Bourenkov, M.A.F. van den Boogaart, L. Doeswijk, J. Brugger, and J.C. Greer, *Microelectron. Eng.* **84**, 42 (2007).
- <sup>30</sup> M. Reinke, Y. Kuzminykh, and P. Hoffmann, *Thin Solid Films* **563**, 56 (2014).
- <sup>31</sup> M.-G. Kim and H.-J. Pahk, *J. Soc. Inf. Disp.* **25**, 249 (2017).
- <sup>32</sup> V.E. de Matos Loureiro da Silva Pereira, J.R. Nicholls, and R. Newton, *Surf. Coat. Technol.* **311**, 307 (2017).
- <sup>33</sup> C. Li, S. Song, D. Gibson, D. Child, H. on Chu, and E. Waddell, *Appl. Opt.* **56**, C65 (2017).

- <sup>34</sup> K. Ono, H. Shimada, S. Kobayashi, and Y. Ootuka, *Jpn. J. Appl. Phys.* **35**, 2369 (1996).
- <sup>35</sup> M.M. Deshmukh, D.C. Ralph, M. Thomas, and J. Silcox, *Appl. Phys. Lett.* **75**, 1631 (1999).
- <sup>36</sup> L. Holland and W. Steckelmacher, *Vacuum* **2**, 346 (1952).
- <sup>37</sup> J.A. Thornton, *J. Vac. Sci. Technol. Vac. Surf. Films* **4**, 3059 (1986).
- <sup>38</sup> Y.G. Yang, R.A. Johnson, and H.N.G. Wadley, *Acta Mater.* **45**, 1455 (1997).
- <sup>39</sup> Y. Golan, L. Margulis, and I. Rubinstein, *Surf. Sci.* **264**, 312 (1992).
- <sup>40</sup> J. Yu and J.G. Amar, *Phys. Rev. E* **66**, (2002).
- <sup>41</sup> Ramanujan, S, *Quart J Math* **45**, 350 (1914).
- <sup>42</sup> <https://Keisan.Casio.Com/Exec/System/1343722259> (n.d.).
- <sup>43</sup> J.M. Kontio, J. Simonen, J. Tommila, and M. Pessa, *Microelectron. Eng.* **87**, 1711 (2010).
- <sup>44</sup> M.T. Taschuk, M.M. Hawkeye, and M.J. Brett, in *Handb. Depos. Technol. Films Coat.* (Elsevier, 2010), pp. 621–678.
- <sup>45</sup> W.P. Davey, *Phys. Rev.* **25**, 753 (1925).
- <sup>46</sup> A.K. Mahapatro, A. Scott, A. Manning, and D.B. Janes, *Appl. Phys. Lett.* **88**, 151917 (2006).
- <sup>47</sup> F.C.M.J.M. van Delft, J.P. Weterings, A.K. van Langen-Suurling, and H. Romijn, *J. Vac. Sci. Technol. B Microelectron. Nanometer Struct.* **18**, 3419 (2000).